Journal of Molecular Liquids 253 (2018) 119–126

Contents lists available at ScienceDirect

Journal of Molecular Liquids

journal homepage: www.elsevier.com/locate/molliq

Study of linear and nonlinear optical properties of nickel immobilized on acid-activated montmorillonite and copper ferrite nanocomposites

Akbar Jafari [a,*], Behzad Zeynizadeh [b], Shiba Darvishi [a]

[a] Atomic and Molecular Group, Department of Physics, Faculty of Science, Urmia University, Urmia 5756151818, Iran
[b] Faculty of Chemistry, Urmia University, Urmia 5756151818, Iran

ARTICLE INFO

Article history:
Received 6 September 2017
Received in revised form 30 December 2017
Accepted 3 January 2018
Available online 04 January 2018

Keywords:
Nonlinear optics
Z-scan technique
Nickel nanoparticles
Montmorillonite
$CuFe_2O_4$

ABSTRACT

In this paper, the third-order nonlinear optical properties of nickel immobilized on acid-activated montmorillonite (MMT@Ni) and copper ferrite ($CuFe_2O_4$@Ni) nanocomposites were investigated. The mentioned nanomaterials were synthesized and then characterized using FT-IR, SEM, EDX, XRD, VSM, and TEM analyses. The nonlinear absorption and refractive coefficients of these nickel nanocomposites were measured by *Z*-scan technique through a continuous wave diode-pumped laser at 532 *nm* wavelength. The values of nonlinear absorption and refractive indexes of samples were obtained in order of $10^{-4} m/w$ and $10^{-10} m^2/w$, respectively. In addition, the sign of nonlinear refractive index for MMT@Ni and $CuFe_2O_4$@Ni was shown to be positive and negative, respectively. It seems that the difference in activities of nanocomposites was relevance to their structural frameworks. Nickel immobilized on acid-activated montmorillonite has layered structure and this provides the possibility to focus the laser beams, and so self-focusing phenomenon was happened. Whereas, nickel immobilized on copper ferrite has inverse spinel structure and this provides the possibility to diverge the laser beams, and so self-defocusing phenomenon was taken place. The results also showed that the values of nonlinearity for solution of $CuFe_2O_4$@Ni and MMT@Ni nanoparticles were respectively increased and decreased by rising of the input intensity. In addition, we found that the support of nickel nanoparticles could change the sign of nonlinear optical behavior.

1. Introduction

Nanostructured materials are one of the highest profile classes of materials in science and engineering and provide the greatest potentials for improving performance and extended capabilities of products in aerospace, drug delivery devices, tooling, automotive, more efficient solar panels, recording, cosmetics, electric motors and refrigeration industries. So, multidisciplinary materials such as multilayer films, atomic clusters, nanocrystalline materials and nanocomposites have remarkable variations in electric, optic and magnetic properties. Their uniqueness is due partially to the very large percentage of atoms at interfaces and partially to quantum confinement effects [1,2].

Among nanocomposite systems, montmorillonite and spinel ferrites are the frequently used materials for numerous applications. Montmorillonite is a very soft phyllosilicate group of minerals that known as clay [3,4]. It is a member of the smectite group and is a 2:1 clay, meaning that it has two tetrahedral sheets of silica sandwiching a central octahedral sheet of alumina. The particles are plate-shaped with an average diameter around 1 μm and a thickness of 9.6 nm. Chemically, it is hydrated sodium calcium aluminium magnesium silicate hydroxide $(Na,Ca)_{0.33}(Al,Mg)_2(Si_4O_{10})(OH)_2 \cdot nH_2O$. It has a cation exchange capacity due to isomorphous substitution of Mg for Al in the central alumina plane. Montimorillonite has been found numerous applications in research and industrial points of view [5–10]. Spinel ferrites is also one of nanocomposite systems that have important applications in drug delivery, electronic devices, medical diagnostics, sensor technology, ferro fluids technology and catalysts, as well as a solid support for a variety of homogeneous catalysts. Spinel ferrites have a general formula of MFe_2O_4 (M: Zn^{2+}, Cu^{2+}, Mg^{2+} and Ni^{2+}) [11,12].

In another hand, materials with high nonlinear optical characteristics and fast nonlinear responses have wide applications in optical instruments technology such as optical switches and optical limiters. Especially, if this nonlinear optics features of materials can be controlled by an external agent. Experimental and theoretical studies showed that the optical properties of some nonlinear materials can be changed by an external electric field or magnetic field [13,14].

In particular, nickel nanoparticles show a high level of surface energy, high magnetism, low melting and burning points as well as high surface area [15,16]. In addition, nickel is a versatile catalyst for cracking of methane to carbon nanotubes and hydrogen, partial oxidation and steam reforming [17]. Nickel fluids with super paramagnetic fine

* Corresponding author.
E-mail address: a.jafari@urmia.ac.ir (A. Jafari).

https://doi.org/10.1016/j.molliq.2018.01.021
0167-7322/

particles behave as Newtonian fluids [17]. The literature review shows that due to superior characteristics of nickel, studies on nonlinear optical property of nickel or its composite systems has attracted a great deal of attentions. In this context, Jiménez-Marín et al. [18] studied a contrasting response in the photoelectrical properties of nickel oxide decorated multiwall carbon nanotubes. Several studies such as; the investigation on third-order nonlinearity of nickel oxide nanoparticles [19], nonlinear optical transmission of surface-modified nickel sulfide nanoparticles [20], optical nonlinearity in $NiFe_2O_4$ nanoparticle [21], nonlinear and magneto-optical transmission studies on magnetic nanofluids of non-interacting metallic nickel nanoparticles [22], nonlinear optical properties of Ni/NiO and $Ni/NiCo_2O_4$ nanocomposites [23], nonlinear optical refraction of Al_2O_3 single crystal doping with nickel nanoparticles [24] and optical dispersion, permittivity spectrum and thermal-lensing effect in nickel-doped zinc sulfide nanoparticles [25] also showed the importance of nickel nanoparticles in nonlinear optical studies.

In line with the outlined strategies and due to lack of information to study the influence of support framework on nonlinear optical properties of nickel nanoparticles, herein, we wish to report the nonlinear optical properties of nickel immobilized on acid-activated montmorillonite (MMT@Ni) and copper ferrite ($CuFe_2O_4$@Ni) nanocomposites. The nonlinear absorption and refractive coefficients of these nanocomposites were calculated using *Z*-scan technique in hydrochloric acid with concentration of 3×10^{-4} M. Nonlinear refractive index, n_2, of the nanoparticles could be obtained through the self-focusing and self-defocusing effects. So, it is important to measure this quantity precisely, in terms of sign and magnitude, for our practical purposes.

2. Experimental

2.1. General

All chemicals were purchased from chemical companies with the best quality and they were used without further purification. FT-IR spectra were recorded on Thermo Nicolet Nexus 670 spectrophotometer. Particle size and morphology of materials were measured by using scanning electron microscopy (SEM) and energy dispersive X-ray spectroscopy (EDX). Montmorillonite K10 was purchased from Sigma-Aldrich company with art No. 69866 (pH ~ 3–4, surface area: 250 m^2/g). X-ray diffraction (XRD) measurements were made on a Bruker D8-Advance diffractometer with graphite-monochromatized Cu Kα radiation (λ = 1.54056 Å) at room temperature. Diffraction patterns were also recorded in 2θ range (10–80°). SEM images were determined on FESEM–TESCAN MIRA3 instrument. Transmission electron microscope (TEM) images were recorded with a Philips CM30 at electron energy of 300 keV. Magnetic properties of the samples were determined using a vibration sample magnetometer (VSM, Meghnatis Daghigh Kavir Co, Kashan, Iran) under magnetic fields up to 20 kOe. The amounts of Cu, Fe and O were measured by inductively coupled plasma-optical emission spectrometry (ICP-OES, Varian 730-ES). Some experimental data and spectra are also available in supporting information (SI).

2.2. Preparation of homoionic Na^+-exchanged montmorillonite

In a beaker (250 mL) containing distilled water (200 mL), montmorillonite K10 (5 g) was added and the mixture was stirred vigorously at room temperature for 20 h. The mixture was then allowed to settle and the aqueous phase was decanted. To the obtained solid residue, an aqueous solution of NaCl (2 M, 200 mL) was added and the mixture was continued to stirring for 2 h at room temperature. The aqueous phase was decanted and the solid residue was again charged with an aqueous solution of NaCl (2 M, 200 mL). After stirring for 2 h at room temperature, the aqueous phase was decanted. The procedure was repeated for additional 2 times. Finally, the solid residue was washed frequently with distilled water until the conductivity of the liquid filtrate reaches to the conductivity of distilled water. The solid residue was dried at 50 °C under air atmosphere to afford homoionic Na^+-exchanged montmorillonite.

2.3. Preparation of nanocomposite nickel immobilized on acid-activated montmorillonite (MMT@Ni)

In a beaker (100 mL) containing an aqueous solution of $Ni(OAc)_2 \cdot 2H_2O$ (0.05 M, 10 mL), acid-activated montmorillonite (0.5 g) was added slowly and the resulting mixture was stirred vigorously at room temperature for 6 h. The aqueous phase was then evaporated under reduced pressure. The dried Mont-$Ni(OAc)_2$ was dispersed in ethylene glycol (50 mL) within a double necked round-bottom flask. The mixture was stirred under reflux and nitrogen atmosphere for 6 h. Ethylene glycol was then removed by decantation and the solid material was washed with MeOH to remove ethylene glycol completely. The obtained composite material was then dried under flowing of nitrogen (12 h) at 40 °C to afford nanocomposite nickel immobilized on acid-activated montmorillonite.

2.4. Preparation of $CuFe_2O_4$ MNPs [26]

In a typical synthesis, analytical grade of $Cu(OAc)_2 \cdot H_2O$, $Fe(NO_3)_3 \cdot 9H_2O$, NaOH, and NaCl were mixed in a molar ratio (1:2:8:2) and ground together in agate mortar for 50 min. The reaction started readily during the mixing process and was accompanied by release of heat. Via the progress of the reaction, the mixture became mushy and underwent gradual changes in color from blue to finally brown. The outcome mixture was washed with deionized water severally. The obtained solid material was then dried at 80 °C for 2 h and calcinated at 300, 500, 600, 700, 800, 900 °C for 2 h to afford magnetically nanoparticles (MNPs) of $CuFe_2O_4$.

2.5. Preparation of $CuFe_2O_4$@Ni MNPs

In a round-bottom flask containing a mixture of $CuFe_2O_4$ MNPs (1 g in 20 mL H_2O), aq. $NiCl_2 \cdot 6H_2O$ (1 mmol, 0.24 g in a 20 mL H_2O) was added. The mixture was stirred vigorously in an ultrasonic bath (100 W) for 30 min. Through a separator funnel, aq. $NaBH_4$ (0.205 g in 25 mL in H_2O) was added and the resulting mixture was stirred for 30 min under nitrogen atmosphere. The black solid precipitate was collected with external magnet and then washed severally with deionized water. Drying under air atmosphere affords magnetically nanocomposite of nickel immobilized on copper ferrite.

2.6. The Z-scan technique

Z-scan technique was presented for measuring nonlinear optical properties of materials by Sheikh Bahaei and his colleagues in 1989 [27]. Nonlinear absorption and refraction coefficients can be measured using this technique [28]. Schematic diagram of the experimental setup for *Z*-scan technique is shown in Fig. 1. In this figure, *BS* is a beam splitter. A continuous wave diode-pumped laser at 532 *nm* wavelength and with Gaussian spatial profile is focused by a convex lens (f = 10 *cm*). The beam radius at the focal plane is about 327*μm*, and the Rayleigh range that is obtained from the equation $z_0 = k\omega_0^2/2$ is 63.25 *mm*. The thickness of the sample is 6.89 *mm* that is less than the Rayleigh range of the beam so the medium can be considered to be thin. The sample was moved from $(-z)$ to $(+z)$. The fraction of diffracted intensity was measured by photodiode 1 in the closed aperture, and photodiode 2 measured the intensity dependant absorption in the open aperture. When a high intensity laser beam passes through a nonlinear material, according to the intensity dependence of the coefficient of refraction, $n_2 = n_0 + n_2 I$ [29,30], the case of $n_2 > 0$ and $n_2 < 0$ causes the occurrence of the phenomena of self-focusing and self-defocusing, respectively. In Fig. 1, for $n_2 > 0$, when the sample is before the focal point of the lens,

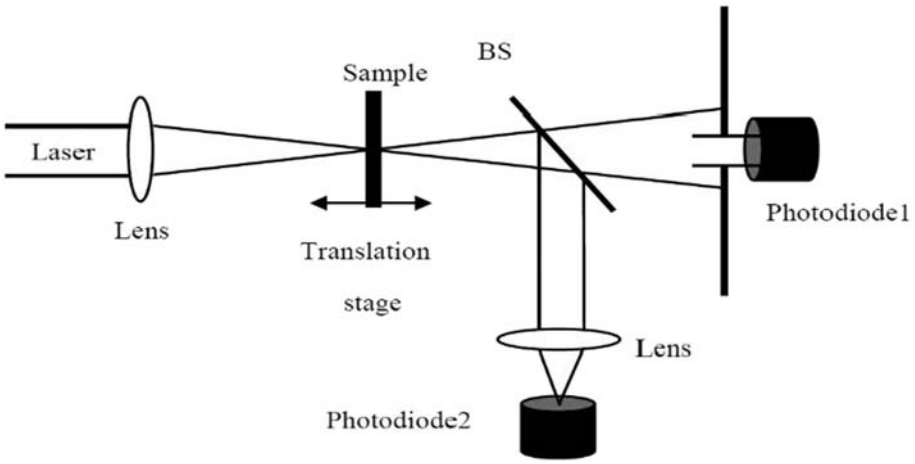

Fig. 1. Experimental setup of *Z*-scan technique.

the transverse section of the laser beam due to self-focusing effect is enlarged on the aperture (in the front of photodiode 1), and transmittance of the aperture decreases. In result, we will have a valley in the transmittance of the aperture when the sample is scanned in the $z < 0$ zone. On the Other hand, after the focal point of the lens, the self-focusing phenomenon causes the transverse section of the laser beam to be smaller in the aperture and will result in the formation of a peak in the $z < 0$ region. With the same argument and in the case of $n_2 < 0$, we will have a peak in the curve of the transmittance of the aperture at $z > 0$ and a valley in the $z < 0$ zone, respectively, due to the self-defocusing phenomenon.

Furthermore, when the sample is swept along the z axis and is passed through the focal point of the lens, the intensity of the laser in the cross section of the beam increases and the data recorded by photodiode 2 shows a valley or a peak in the position of $z = 0$. This phenomenon is due to the dependence of sample absorption coefficient to the laser intensity, $\alpha = \alpha_0 + \beta I$ [30]. As if in this relation $\beta > 0$, we will see a valley, due to occurrence of nonlinear two photon absorption, and in the case of $\beta < 0$, we will see a peak, due to nonlinear saturable absorption.

The nonlinear refraction coefficient was calculated by [29],

$$n_2 = \Delta\phi / k I_0 L_{eff} \tag{1}$$

where, $k = \frac{2\pi}{\lambda}$ is the wave vector and λ is the laser wave length, I_0 is the intensity of the laser beam at the focus, $L_{eff} = \frac{(1-e^{-\alpha L})}{\alpha}$ is the sample's effective length and α is the linear absorption that its values are given in Table 1, and $\Delta\phi$ is the nonlinear phase shift of the transmittance of laser beam and is related to the normalized transmittance difference of peak and valley, $\Delta T_{(P-V)}$ by [29],

$$\Delta T_{(P-V)} = 0.406(1-S)^{0.25}\Delta\phi \tag{2}$$

where, S is the linear aperture transmittance and can be determined by,

$$S = 1 - exp(-2r_a^2/\omega_a^2) \tag{3}$$

here, r_a is the aperture radius and ω_a is the beam radius on the aperture.

Table 1
The measured values of light transmission and linear absorption of MMT@Ni and $CuFe_2O_4$@Ni nanocomposites in hydrochloric acid with concentration of 3×10^{-4} M.

Samples	T	$\alpha\,(cm^{-1})$
MMT@Ni	0.9795	0.0207
$CuFe_2O_4$@Ni	0.9954	0.0046

From the best fitting equation, performed on the experimental and theoretical data of the open aperture measurement, the nonlinear absorption coefficients $\beta(m/w)$ can be determined. These fittings can be plotted by,

$$\Delta T(z) \approx 1 - \frac{q_0}{2\sqrt{2}} \frac{1}{\left(1 + (z/z_0)^2\right)} \tag{4}$$

In this relation, $\Delta T(z)$ is the normalized transmittance of the sample at z and z_0 is the Rayleigh diffraction length. The values of β can be calculated by,

$$q_0 = \beta I_0 L_{eff} \tag{5}$$

The values of $\Delta T_{(P-V)}$ and $\Delta T(z)$ are normalized to the values of photodiode1 and photodiode2 data, respectively, when the sample is far from the focal point of the lens.

The values of the real and imaginary parts and the magnitude of third-order nonlinear susceptibility $\chi^{(3)}$ are calculated by [31],

$$Re\chi^{(3)}(esu) = \frac{10^{-4}\varepsilon_0 c^2 n_0^2}{\pi} n_2 (cm^2/w) \tag{6}$$

$$Im\chi^{(3)}(esu) = \frac{10^{-2}\varepsilon_0 c^2 n_0^2 \lambda}{4\pi^2} \beta(cm/w) \tag{7}$$

$$|\chi^{(3)}| = \left[\left(Re\left[\chi^{(3)}\right]\right)^2 + \left(Im\left[\chi^{(3)}\right]\right)^2\right]^{\frac{1}{2}} (esu) \tag{8}$$

In these equations, ε_0 is the electric permittivity of free space ($8.85 \times 10^{-12}\,\frac{F}{m}$), c is the velocity of light in vacuum and n_0 is the linear refractive index of each sample.

2.7. UV–Vis absorption spectra

The solutions for nanoparticles were prepared in hydrochloric acid with concentration of 3×10^{-4} M and then placed in quartz cell. The linear absorption of these nanoparticles was measured by using a spectrophotometer. The linear absorption spectra of these nanoparticles are shown in Fig. 1-SI. The linear absorption coefficients of them have been calculated by,

$$\alpha = -\frac{1}{d} LnT \tag{9}$$

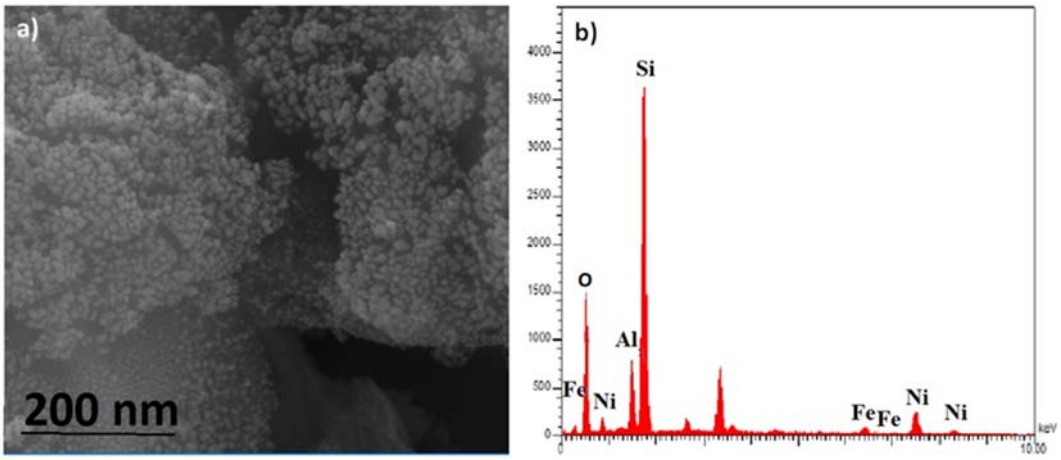

Fig. 2. a) SEM and b) EDX spectra of MMT@Ni.

In this equation, α is the linear absorption coefficient of the sample, $d = 1\ cm$ is the cell thickness and T is the transmission of light. The values of the linear absorption coefficients of these nanoparticles are listed in Table 1.

3. Results and discussion

3.1. Synthesis of nanocomposite nickel immobilized on acid-activated montmorillonite (MMT@Ni)

The study was started primarily by nanocomposite synthesis of nickel immobilized on montmorillonite (MMT@Ni) in a five-step procedure: i) preparation of swelled (hydrated) montmorillonite through the vigorous stirring of commercially available montmorillonite K10 in distilled water, ii) preparation of homoionic Na^+-exchanged montmorillonite by adequate stirring of the swelled montmorillonite in an aqueous solution of NaCl, iii) preparation of acid-activated montmorillonite by stirring of homoionic Na^+-exchanged montmorillonite in an aqueous solution of HCl, iv) preparation of the immobilized $Ni(OAc)_2$ on acid-activated montmorillonite by a simply mixing and stirring of acid-activated montmorillonite in an aqueous solution of nickel acetate, and finally v) reduction of nickel acetate to Ni(0) with ethylene glycol to obtain the final nanocomposite of MMT@Ni.

After nanocomposite synthesis of MMT@Ni, the size and morphology of montmorillonite K10 (Mont K10), acid-activated montmorillonite (H-Mont) and nickel immobilized montmorillonite (MMT@Ni) was studied using FT-IR, scanning electron microscopy (SEM) and energy dispersive X-ray spectroscopy (EDX).

The illustrated FT-IR spectra (Fig. 2-SI) exhibited that Mont K10 shows a strong absorption band at 1054 cm^{-1} indicating Si-O stretching vibrations of tetrahedral sites. The bands at 522 and 464 cm^{-1} are also attributed to Si–O–Al and Si–O–Si bending vibrations. Through the acid activation of montmorillonite, the band at 1054 cm^{-1} is shifted to 1080 cm^{-1}. A small band near 795 cm^{-1} is due to amorphous silica. Mont K10 also shows absorption bands at 3620 and 1635 cm^{-1} that are attributed to stretching and bending vibrations of OH groups of Al–OH. By immobilization of Ni(0) on montmorillonite, some changes in absorption bands of the parent spectra were also happened.

SEM images and EDX spectra of Mont K10 and H-Mont are shown in Fig. 3-SI. The images (Figs. 3a-SI and 3c-SI) show that via the acid activation, the layered construction of Mont K10 is exfoliated to tiny segments. This transformation is attributed to the elimination of major contents of Al from octahedral sites by the reaction with HCl. In addition, elimination of Al contents generates new pores on the surface and internal layers of montmorillonite leading to increase specific surface area.

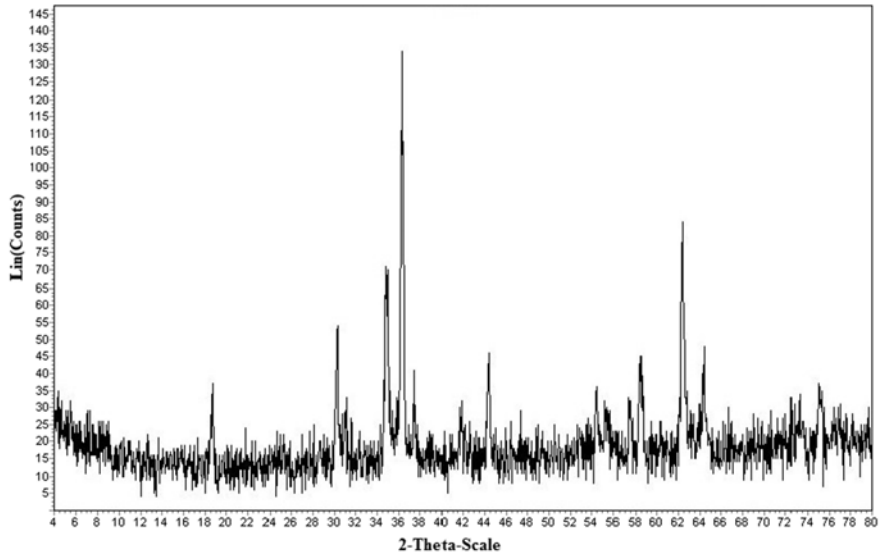

Fig. 3. XRD spectrum of $CuFe_2O_4$ MNPs.

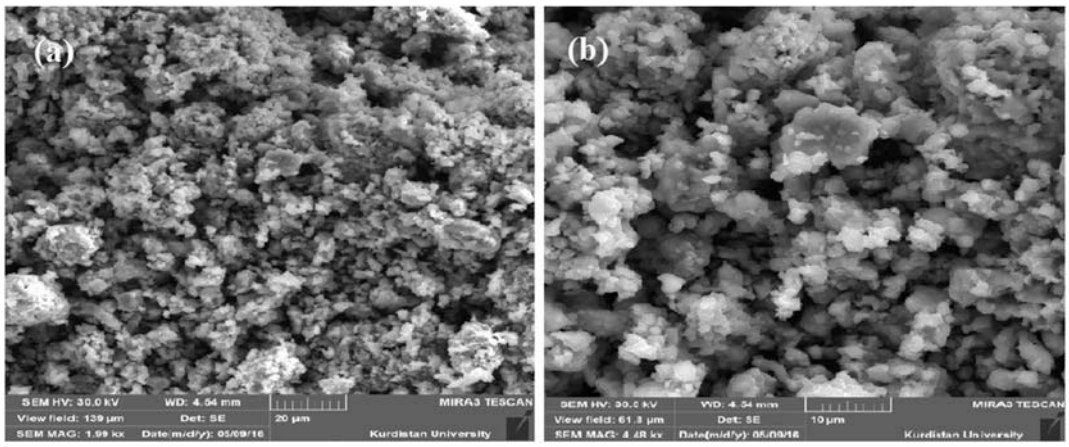

Fig. 4. SEM images of $CuFe_2O_4$ MNPs.

SEM image of MMT@Ni (Fig. 2a) reveals that the immobilized particles have spherical shapes and well dispersed in the pores and surface of tiny segments with a particle size of 10–20 nm. EDX analysis (Fig. 2b) also indicates that Ni(0) nanoparticles as well as other elements are present in the final clay composite.

3.2. Synthesis of $CuFe_2O_4$@Ni MNPs

The preparation of $CuFe_2O_4$ MNPs by solid-state grinding of $Cu(OAc)_2 \cdot H_2O$, $Fe(NO_3)_3 \cdot 9H_2O$, NaOH and NaCl in a molar ratio 1:2:8:2 was taken place according to the reported procedure [26]. The process is ecofriendly, economical and very efficient. The prepared $CuFe_2O_4$ MNPs was then characterized by Fourier transform infrared spectroscopy (FT-IR), X-ray diffraction (XRD), scanning electron microscopy (SEM), transmission electron microscopy (TEM), energy-dispersive X-ray spectroscopy (EDX), inductively coupled plasma-optical emission spectrometry (ICP-OES), vibrating sample magnetometer (VSM) analyses.

Fig. 4-SI shows the recorded FT-IR spectrum for the prepared sample of $CuFe_2O_4$ MNPs. In this spectrum, two main absorption bands at 586.88 and 405.82 cm^{-1} are attributed to stretching vibrations of Cu—O bonds in tetrahedral and octahedral sites of cubic spinel ferrite. It is notable that the stretching absorption band of Cu—O in tetrahedral sites, because of short bond length of Cu—O, were appeared at a higher wave number in comparison to octahedral sites.

The recorded XRD spectrum for $CuFe_2O_4$ MNPs (Fig. 3) shows that all the peaks in the spectrum matched well with the standard one of copper ferrite (JCPDS 34-0425). The appeared peaks at $2\Theta = 18.91°$, 31.02°, 36.62°, 38.38°, 44.92°, 55.62°, 58.48° and 62.19° were indexed to (111), (220), (311), (222), (400), (422), (511), and (440) crystal planes of spinel ferrite, respectively. In addition, the pattern represents that the nanomagnetic $CuFe_2O_4$ has a cubic unit cell with inverse spinel crystals.

The morphology and size distribution of $CuFe_2O_4$ MNPs was also determined using scanning electron microscopy (SEM) and transmission electron microscopy (TEM). Fig. 4a and b represent SEM images, and Figs. 5a-SI and 5b-SI show TEM images of the prepared sample. The images show that the copper ferrite nanocomposite has an irregular morphology. The size of $CuFe_2O_4$ particles was found to be 13–29 nm.

The elemental (Cu, Fe, and O) composition of $CuFe_2O_4$ MNPs was determined by energy dispersive X-ray spectroscopy (EDX). Fig. 6-SI shows that all the titled elements are present in the nanocomposite. Through the inductively coupled plasma-optical emission spectrometry (ICP-OES), the amounts of Cu, Fe and O in $CuFe_2O_4$ MNPs were determined 22.52%, 46.71% and 30.77%, respectively.

Magnetic property of $CuFe_2O_4$ nanoparticles was also investigated at room temperature by vibrating sample magnetometer (VSM) analysis. The obtained saturation magnetization value ($Ms = 38\ emu \cdot g^{-1}$) and shape of the illustrated pattern shows that the prepared sample has a paramagnetic characteristic for a good magnetic separation (Fig. 5).

The recorded XRD spectrum for $CuFe_2O_4$@Ni MNPs (Fig. 6) shows that the spectrum involves the peaks for XRD spectrum of $CuFe_2O_4$ (Fig. 3) and Ni nanoparticles. In addition, the recorded pattern represents that the nanomagnetic $CuFe_2O_4$@Ni has a cubic unit cell with inverse spinel crystals.

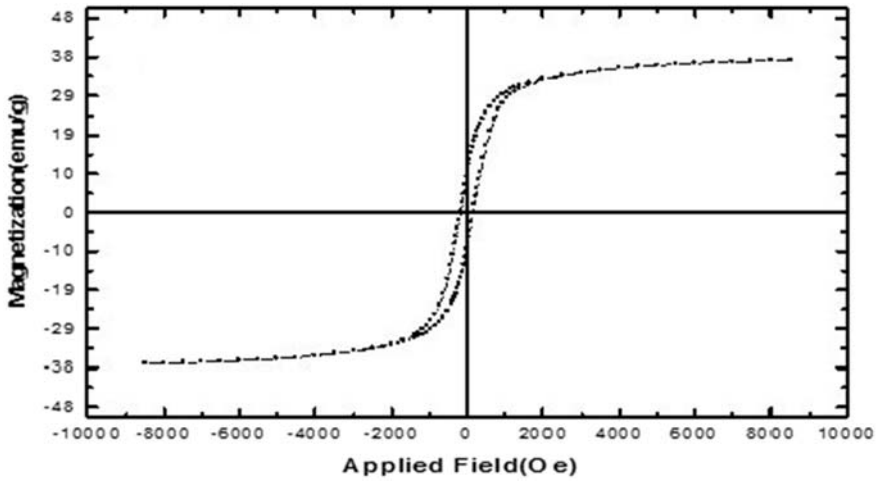

Fig. 5. VSM spectrum of $CuFe_2O_4$ MNPs.

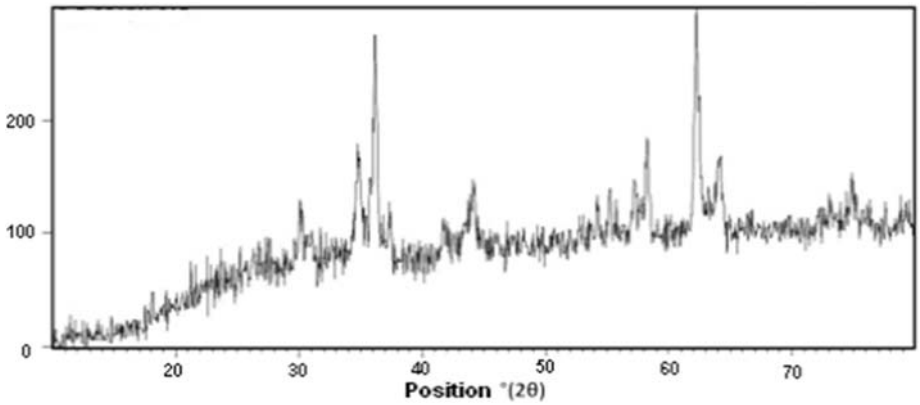

Fig. 6. XRD spectrum of $CuFe_2O_4$@Ni MNPs.

3.3. Z-scan results of $CuFe_2O_4$@Ni and MMT@Ni

Fig. 7a and b show the closed aperture Z-scan signal $\Delta T_{(P-V)}$ at the laser intensity of $I_\circ = 54.21 \times 10^3 \frac{w}{m^2}$ for MMT@Ni and $CuFe_2O_4$@Ni, respectively. The same closed aperture Z-scan curves at $I_\circ = 70.90 \times 10^3 \frac{w}{m^2}$ were also illustrated in Figs. 7a-SI and 7b-SI for MMT@Ni and $CuFe_2O_4$@Ni, respectively. According to the Fig. 7a and Fig. 7a-SI, there is a pre-focal minimum (valley) which is followed by a post-focal maximum (peak) in transmittance indicating positive nonlinearity with a self-focusing effect. However in Fig. 7b and Fig. 7b-SI, the pre-focal maximum (peak) is followed by a post-focal minimum (valley) in transmittance, showing negative nonlinearity with a self-defocusing effect. At the closed aperture, Eq. (1) was used to calculate the intensity-dependence of nonlinear refraction processes of nanoparticles.

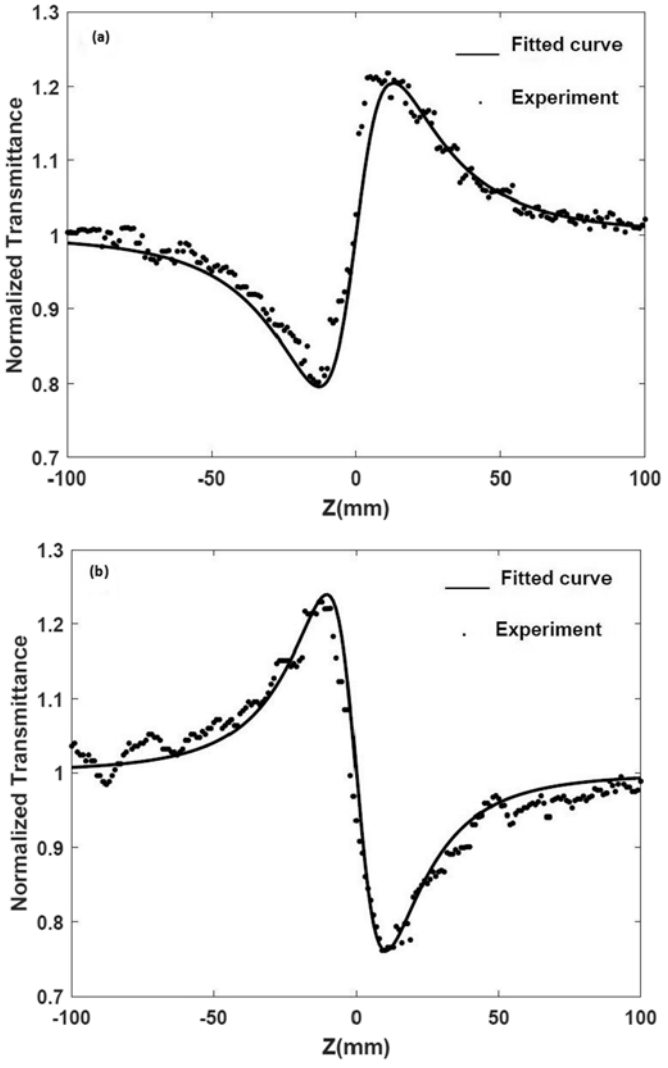

Fig. 7. Closed aperture *Z*-scan curves of a) MMT@Ni and b) $CuFe_2O_4$@Ni in HCl 3×10^{-4} M at $I_\circ = 54.21 \times 10^3 \frac{w}{m^2}$.

By studying the intensity-dependent refraction coefficients of these nanoparticles in two intensities of the laser beams and in hydrochloric acid 3×10^{-4} M, it is observed that increasing the intensity leads to increased peak-valley transmittance difference. It can be determined that the theoretical fits to the closed aperture experimental data is given by,

$$T(z) = 1 - \frac{4\Delta\phi(z/z_0)^2}{\left(1+(z/z_0)^2\right)\left(9+(z/z_0)^2\right)} \tag{10}$$

This relation shows an agreement between theory and experimental data and it can be used regarding plate of theoretical fits of experimental curves [32].

The values of nonlinear refractive index of the nanocomposite systems in two different intensities are given in Table 2. It is customary to consider carbon disulfide (CS_2) as a reference material for the nonlinear refractive indexe measurement. Ganeev et al. [33] measured the nonlinear refractive index of CS_2 in the order ~$10^{-14} - 10^{-15}\ cm^2W^{-1}$ in different laser pulls durations, which is at least 10^4 order of magnitude less than the refractive indexes of MMT@Ni and $CuFe_2O_4$@Ni.

The sign of nonlinear refraction for MMT@Ni ($CuFe_2O_4$@Ni) is positive (negative). The difference in the nonlinear refractive index sign of nanocomposites may be due to their supports which create different nonlinear properties. Fig. 8a and b illustrate the difference between activities of two supports. In Fig. 8a, we can observe that the structure of nickel immobilized on acid-activated montmorillonite is a layered structure and this provides the possibility to focus the laser beams and self-focusing phenomenon was happened. However, Fig. 8b shows that nickel immobilized on copper ferrite has an inverse spinel structure

Table 2
Values of intensity and nonlinear refractive index of MMT@Ni and $CuFe_2O_4$@Ni nanocomposites in hydrochloric acid 3×10^{-4} M.

Samples	$I_0\left[\frac{w}{m^2}\right]\left(\times 10^3\right)$	$n_2\left[\frac{m^2}{w}\right]\left(\times 10^{-10}\right)$
MMT@Ni	54.21	2.29
	70.90	2.03
$CuFe_2O_4$@Ni	54.21	2.65
	70.90	2.26

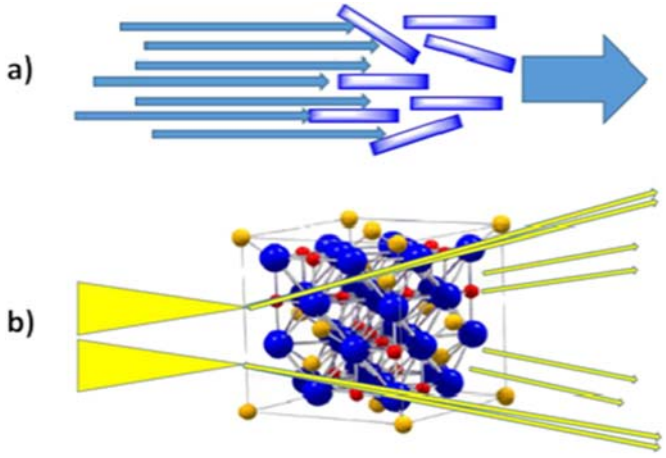

Fig. 8. a) The sheet structure of nickel immobilized on acid-activated montmorillonite and its relation with focusing of laser beams, b) The inverse spinel structure of nickel immobilized on copper ferrite and its relation with divergence of laser beams

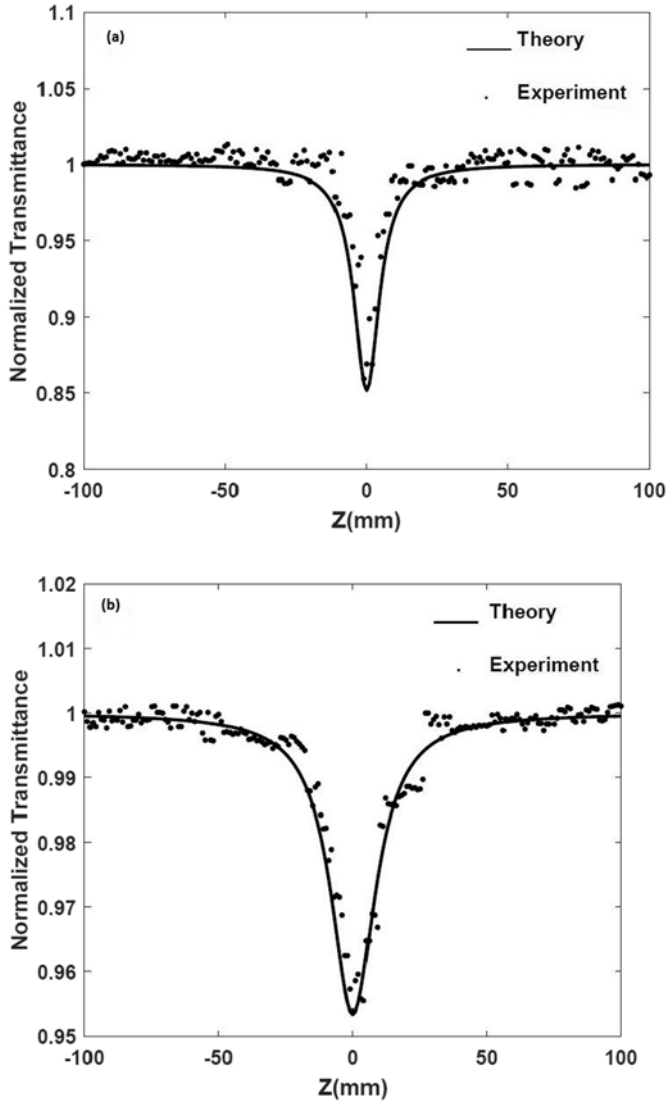

Fig. 9. The open aperture *Z*-scan curves of a) MMT@Mi and b) $CuFe_2O_4$@Ni in HCl 3×10^{-4} M at $I_\circ = 54.21 \times 10^3 \frac{w}{m^2}$.

Table 3
The values of nonlinear absorption coefficient of MMT@Mi and $CuFe_2O_4$@Ni nanocomposites in hydrochloric acid 3×10^{-4}M.

Samples	$I_0\left[\frac{w}{m^2}\right]\left(\times 10^3\right)$	$\beta[m/w](\times 10^{-4})$
MMT@Ni	54.21	11.30
	70.90	2.5
$CuFe_2O_4$@Ni	54.21	3.50
	70.90	1.5

and this provides the possibility to diverge the laser beams and self-defocusing phenomenon was taken place. Furthermore, since the result of cw laser radiation on the materials is thermal effect, the nonlinear response of these materials is related to the gradient of the change in refractive index with temperature (dn/dT). It should be noted that this thermal lensing effect is as self-focusing and self-defocusing phenomena in MMT@Ni and $CuFe_2O_4$@Ni, respectively.

Fig. 9a and b shows the normalized transmittance for the open aperture *Z*-scan as a function of *z* at the laser intensity of $I_\circ = 54.21 \times 10^3 \frac{w}{m^2}$ for nickel immobilized on acid-activated montmorillonite and copper ferrite, respectively. The normalized transmittance for the open aperture Z-scan at $I_\circ = 70.90 \times 10^3 \frac{w}{m^2}$ for nickel immobilized on acid-activated montmorillonite and copper ferrite were also illustrated in Figs. 8a-SI and 8b-SI, respectively. From the best fitting equation, performed on the experimental and theoretical data of the open aperture measurement the nonlinear absorption coefficients $\beta(m/w)$ can be determined. These fittings can be plotted by,

$$\Delta T(z) \approx 1 - \frac{q_0}{2\sqrt{2}} \frac{1}{\left(1 + (z/z_0)^2\right)} \tag{11}$$

In this equation, $\Delta T(z)$ is the normalized transmittance of the sample at *z* and z_0 is the Rayleigh diffraction length. The values of β can be calculated by Eq. (5).

For both of the samples, existence of a valley in the curve shows that two-photon absorption has occurred. The values of nonlinear absorption are decreased when the intensity of laser beam increases. It may be due to saturable absorption. The values of nonlinear absorption coefficients of these nanoparticles are given in Table 3.

The values of the real and imaginary parts and magnitude of the third-order nonlinear optical susceptibility $\chi^{(3)}$ are given in Table 4.

As seen from Table 4, the studied nanocomposite systems shows magnitudes of third-order nonlinear susceptibility as large as 10^{-9} esu in the line of 532 nm wavelength of laser beam. Thus they can have a great potential in application of optical devices such as optical switching. Suitability for this application can be considered by a parameter as figure of merit ($FOM = n_2 I_0/\alpha_0 \lambda$) which is proportional to the ratio of nonlinear optical response to the linear absorption in a certain wavelength, that should be >1 [34]. By using data (Tables 1 and 2), the values of FOM for MMT@Ni and $CuFe_2O_4$@Ni were calculated as 11 and 58.7, respectively, at $I_0 = 54.21 (^W/_{m^2})$ and $\lambda = 532$ (nm). So, these nanoparticles especially $CuFe_2O_4$@Ni may be have applications in optical switching.

4. Conclusions

In this paper, the third-order nonlinear optical properties of nickel immobilized on acid-activated montmorillonite and copper ferrite were investigated. The nonlinear refractive index of the nanocomposite systems in hydrochloric acid with concentration of 3×10^{-4} M was measured by *Z*-scan technique and a continuous wave diode-pumped laser. The values of nonlinear refractive index of these nanoparticles

Table 4
The values of linear and nonlinear refractive index, and nonlinear optical susceptibility of the nanocomposite systems in different laser intensities.

Samples	(n_0)	$I_0[w/m^2](\times 10^3)$	$n_2[m^2/w](\times 10^{-10})$	$Re\chi^{(3)}[esu](\times 10^{-8})$	$Im\chi^{(3)}[esu](\times 10^{-8})$	$\lvert\chi^{(3)}\rvert[esu](\times 10^{-8})$
MMT@Ni	1.382	54.21	2.29	1.11	23.20	23.22
$CuFe_2O_4$@Ni	1.383	70.90	2.26	1.09	3.08	3.27

are gained from the order of $10^{-10}m^2/w$. When the input intensity was increased, nonlinear refractive index of $CuFe_2O_4$@Ni was increased and in the case of MMT@Ni was decreased. The sign of nonlinear refractive index for MMT@Ni is positive and for $CuFe_2O_4$@Ni is negative. The difference in signs may be influenced by their structural frameworks. Nickel immobilized on acid-activated montmorillonite has a layered construction and this provides the possibility to focus the laser beams and self-focusing phenomenon was happened. Whereas nickel immobilized on copper ferrite has an inverse spinel structure and this provides the possibility to diverge the laser beams and self-defocusing phenomenon was taken place. In another hand, the results of Tables 3 and 4 show that the nonlinear absorption and the imaginary part of third order susceptibility of sample 1 is one order of magnitude greater than of sample 2. The reason for this can be found in the results of Fig. 1-SI. As shown in this figure, both samples have a strong linear absorption near 266 nm, with the difference that the linear absorption of MMT@Ni is greater than $CuFe_2O_4$@Ni. Therefore, the difference in the nonlinear absorption (two-photon absorption at 532 nm) seems to be rooted in the deference of linear absorption coefficients of the samples at 266 nm. One of the most important advantages of these nanocomposite systems is their high nonlinearity in respect to the reference nonlinear material (CS_2) and also the ability to change of their sign of nonlinear refractive index relative to the different supports. Furthermore, having a large figure of merit parameter in the examined materials makes them a good candidate for use in the optical switching devices.

Acknowledgements

The authors gratefully appreciated the financial support of this work by the research council of Urmia University.

Appendix A. Supplementary data

Supplementary data to this article can be found online at https://doi.org/10.1016/j.molliq.2018.01.021.

References

[1] P. Moriarty, Rep. Prog. Phys. 64 (2001) 297–381.
[2] C.C. Koch, Nanostructured Materials: Processing, Properties and Applications, 2nd ed. William Andrew Inc., 2007
[3] https://en.wikipedia.org/wiki/Montmorillonite, Accessed date: 18 December 2017.
[4] A. Gil, S.A. Korili, R. Trujillano, M.A. Vicente, Pillared Clays and Related Catalysts, Springer, New York, 2010.
[5] K.G. Bhattacharyya, S.S. Gupta, Adv. Colloid Interf. Sci. 140 (2008) 114–131.
[6] L. Lloyd, Handbook of Industrial Catalysts, Springer, New York, 2011 181–182.
[7] G. Nagendrappa, Appl. Clay Sci. 53 (2011) 106–138.
[8] J.H. Clark, C.N. Rhodes, Clean Synthesis Using Porous Inorganic Solid Catalysts and Supported Reagents, Royal Society of Chemistry, Cambridge, 2000.
[9] J.H. Clark, A.P. Kybett, D.J. Macquarrie, Supported Reagents: Preparation, Analysis, and Applications, VCH, New York, 1992.
[10] R.S. Varma, Tetrahedron 58 (2002) 1235–1255.
[11] https://en.wikipedia.org/wiki/Spinel_group, Accessed date: 18 December 2017.
[12] J. Tan, W. Zhang, A.L. Xia, Mater. Res. 16 (2013) 237–241.
[13] A. Jafari, H. Tajalli, A. Ghanadzadeh, Opt. Commun. 266 (2006) 207–213.
[14] J.P. Huang, K.W. Yu, Appl. Phys. Lett. 86 (2005), 041905. .
[15] Q. Zhang, Y. Kusaka, X. Zhu, K. Sato, Y. Mo, T. Kluz, K. Donaldson, J. Occup. Health 45 (2003) 23–30.
[16] D.J. Sivulka, Regul. Toxicol. Pharmacol. 43 (2005) 117–133.
[17] J.C. De Jesús, I. González, M. García, C. Urbina, J. Vac. Sci. Technol. A 26 (2008) 913–918.
[18] E. Jiménez-Marín, I. Villalpando, M. Trejo-Valdez, F. Cervantes-Sodi, J.R. Vargas-García, C. Torres-Torres, Mater. Sci. Eng. B 220 (2017) 22–29.
[19] L.A. Gómez, C.B. de Araújo, L.M. Rossi, S.H. Masunaga, R.F. Jardim, Opt. Lett. 32 (2007) 1435–1437.
[20] V.S. Muthukumar, J.K. Kiran, J. Reppert, R. Satyajit, V. Krishna, G. Nageshwar Rao, S.S. Rama Krishnan, S.S. Sankara Sai, K. Venkataramaniah, A.M. Rao, Nano 3 (2008) 161–167.
[21] K. Sridharan, M. Agarwal, J. Philip, T. Endo, R. Philip, Trans. Mater. Res. Soc. Jpn. 35 (2010) 159–162.
[22] A.P. Reena Mary, C.S. Suchand Sandeep, T.N. Narayanan, R. Philip, P. Moloney, P.M. Ajayan, M.R. Anantharaman, Nanotechnology 22 (2011) 375702–375709.
[23] K.M. Rahulan, N. Padmanathan, R. Philip, S. Balamurugan, C.C. Kanakam, Appl. Surf. Sci. 282 (2013) 656–661.
[24] X. Yu, Y. Wang, Y. Wang, Laser Phys. 24 (2014), 055403. .
[25] F. Abbasi, E. Koushki, M.H. Majles Ara, R. Sahraei, J. Electron. Mater. 46 (2017) 6473–6479.
[26] Z. Sun, L. Liu, D.Z. Jia, W. Pan, Sensors Actuators B Chem. 125 (2007) 144–148.
[27] M. Sheik-Bahae, A.A. Said, E.W. van Stryland, Opt. Lett. 14 (1989) 955–957.
[28] Y.–X. Zhang, Y.–H. Wang, RSC Adv. 7 (2017) 45129–45144.
[29] W.R. Boyd, Nonlinear Optics, 3rd ed. Elsevier, Burlington, 2008.
[30] M. Sheik-Bahae, A.A. Said, T.H. Wei, D.J. Hagan, E.W. Van Stryland, IEEE J. Quantum Electron. 26 (1990) 760–769.
[31] S. Valligatla, K.K. Haldar, A. Patra, N.R. Desai, Opt. Laser Technol. 84 (2016) 87–93.
[32] E.W. van Stryland, M. Sheik-Bahae, A.A. Said, D.J. Hagan, Prog. Cryst. Growth Charact. Mater. 27 (1993) 279–311.
[33] R.A. Ganeev, A.I. Ryasnyansky, M. Baba, M. Suzuki, N. Ishizawa, M. Turu, S. Sakakibara, H. Kuroda, Appl. Phys. B Lasers Opt. 78 (2004) 433–438.
[34] G. Li, Q. Ren, X. Wang, T. Li, H. Yang, J. Chen, J. Zhang, Appl. Phys. A Mater. Sci. Process. 104 (2011) 1099–1103.